

OPEN ACCESS

EDITED BY
Julie Mougin,
CEA/LITEN, France

REVIEWED BY

Abhishek Kumar Singh, University of Twente, Netherlands Alberto De La Calle, Spanish National Research Council (CSIC), Spain

*CORRESPONDENCE Alon Lidor, ⋈ alon.lidor@nrel.gov

RECEIVED 14 July 2025 ACCEPTED 15 September 2025 PUBLISHED 07 October 2025

CITATION

Lidor A and Martinek J (2025) REDOTHERM: a thermodynamic modeling framework for redox-based thermochemical processes. *Front. Energy Res.* 13:1665986. doi: 10.3389/fenrg.2025.1665986

COPYRIGHT

© 2025 Lidor and Martinek. This is an open-access article distributed under the terms of the Creative Commons Attribution License (CC BY). The use, distribution or reproduction in other forums is permitted, provided the original author(s) and the copyright owner(s) are credited and that the original publication in this journal is cited, in accordance with accepted academic practice. No use, distribution or reproduction is permitted which does not comply with these terms

REDOTHERM: a thermodynamic modeling framework for redox-based thermochemical processes

Alon Lidor* and Janna Martinek

National Renewable Energy Laboratory, Golden, CO, United States

Two-step thermochemical redox cycles are being developed as a potential pathway for the production of hydrogen and syngas. While there are many possible reactor and system configurations, moving oxide systems are considered promising in terms of the redox thermodynamics, due to the potential implementation of a countercurrent system that can achieve higher performance compared to other configurations. There is a lack of a robust thermodynamic modeling framework in the field, with multiple models incorporating incorrect thermodynamic assumptions that violate the second law of thermodynamics. We present in this work REDOTHERM, an open-source system model for moving oxides that incorporates the correct thermodynamic limits, as well as various options for the system auxiliary units including product separation, heat recovery, and oxygen removal. The model is agnostic to the energy source, and could be used for solar thermal or other configurations. We highlight the uses of this model, presenting some of the tradeoffs and challenges in redox-active material selection and how they affect the entire thermochemical hydrogen production process. This model could be easily adapted and used for material exploration, system/reactor design, and technoeconomic analysis.

KEYWORDS

chemical looping, solar thermochemical hydrogen production, system modeling, advanced water splitting, thermodynamic modeling

1 Introduction

There is a significant growing interest in chemical looping processes where a metal oxide is used as an oxygen carrier in a redox cycle. These processes include chemical looping combustion, chemical looping reforming, chemical looping gasification, and thermochemical fuel production from water and CO_2 (Adanez et al., 2012; Fan, 2011; Kathe et al., 2017; Zhao et al., 2017; Romero and Steinfeld, 2012; Warren and Weimer, 2022). Two-step thermochemical redox cycles provide a route to split water and/or CO_2 driven by thermal rather than electrical inputs, while inherently separating O_2 from H_2 and/or CO products, respectively. Numerous oxide materials have been considered for the process (Scheffe and Steinfeld, 2014; Budama et al., 2022; Warren et al., 2022; Mao et al., 2020). Early efforts focused on oxides that can operate in a two-step cycle and undergo stoichiometric reduction such as ZnO_1 , SnO_2 , SnO_2 , or ferrite materials ($M_xFe_{3-x}O_4$). However, challenges with rapid quenching requirements for volatile oxide materials, sintering, and cyclic stability led to a shift toward non-stoichiometric oxides including CeO_2 , doped CeO_2 , or

various perovskite (ABO₃) materials (Abanades and Flamant, 2006; Chueh et al., 2010; Abanades et al., 2010; Siegel et al., 2013; McDaniel et al., 2013; Scheffe and Steinfeld, 2014). The lattice structure of non-stoichiometric oxides can accommodate anion or cation vacancies, providing fast kinetic rates along with long-term cyclic physical and chemical stability (Chueh et al., 2010).

In a typical two-step non-stoichiometric metal oxide redox cycle, the endothermic reduction of the oxide is carried out as shown in Equation 1 where $\Delta\delta=\delta_{\rm red}-\delta_{\rm ox}$ is the change in non-stoichiometry between the reduced and oxidized states.

$$\frac{1}{\Lambda \delta} M_{x} O_{y - \delta_{ox}} \rightarrow, \frac{1}{\Lambda \delta} M_{x} O_{y - \delta_{red}} + \frac{1}{2} O_{2}$$
 (1)

This is followed by an exothermic oxidation step with either steam or CO_2 in Equation 2 or Equation 3 thereby completing the cycle.

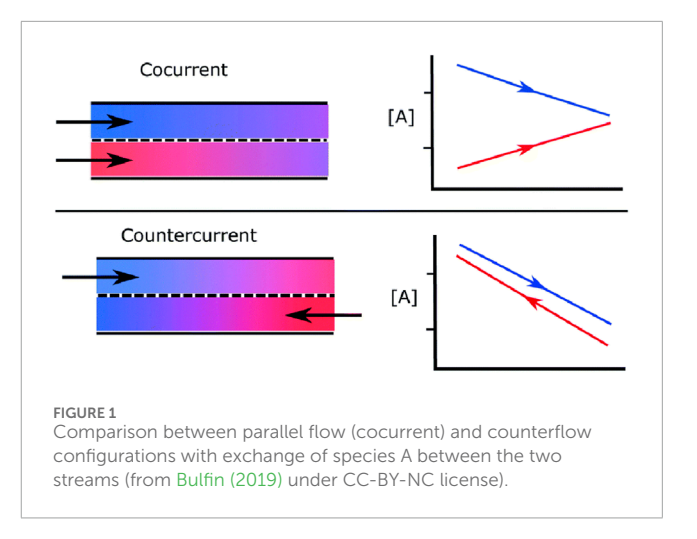
$$\frac{1}{\Lambda\delta}M_{x}O_{y-\delta_{red}} + H_{2}O \rightarrow, \frac{1}{\Lambda\delta}M_{x}O_{y-\delta_{ox}} + H_{2}$$
 (2)

$$\frac{1}{\Lambda \delta} M_{x} O_{y-\delta_{red}} + CO_{2} \rightarrow, \frac{1}{\Lambda \delta} M_{x} O_{y-\delta_{ox}} + CO$$
 (3)

The endothermic reduction reaction is thermodynamically favored at high temperature and low oxygen partial pressure conditions, whereas the exothermic oxidation is thermodynamically favored by comparatively lower temperatures and high steam or CO₂ concentration

The techno-economic potential of chemical looping for H₂ or syngas production can only be realistically evaluated when viewed within the context of the full system including not only the thermochemical reactor(s), but also requirements for all unit operations including heat recuperation, product separations, etc. This presents numerous tradeoffs in the selection of ideal system conditions including target temperature and pressure conditions for each the reduction and oxidation reactors, and relative sweep gas or steam/CO2 flow rates (Li et al., 2018a; Ehrhart et al., 2016; Lidor and Bulfin, 2024). For example, conditions which maximize H₂ or CO productivity per mass of oxide (high reduction temperature, large difference between reduction and oxidation temperatures, large excess of steam or CO2) can lead to low steam or CO2 conversion along with energy- and capital-intensive heat exchange and separation operations. These costs are not trivial, for example, the cost of separation in reverse water-gas shift processes can be more expensive than the reactor itself (Zang et al., 2021). In addition, low feedstock conversion produces low power density, which means larger reactor volumes and a larger mass of redox-active material required to produce a given quantity of product (Lidor and Bulfin, 2024).

Coupling chemical looping redox cycles with concentrated solar thermal (CST) systems was first proposed as a potential pathway for the production of hydrogen during the 1970s (Nakamura, 1977). A myriad of widely-varying reactor concepts exist in the literature, including directly- and indirectly-irradiated designs as well as batch vs. flow-through designs (Steinfeld, 2005; Gokon et al., 2011; Romero and Steinfeld, 2012; Hathaway et al., 2016; Thanda et al., 2022; Budama et al., 2022). Many analyses pair a specific oxide material with a specific reactor design, and the resulting experimental or model-predicted performance combines the underlying material thermodynamics with heat



and mass transfer limitations and characteristics that arise from the reactor design and/or selected operating conditions. These studies can provide valuable comprehensive assessments for the specific combination of oxide material, reactor, and operating conditions; however, there is little opportunity for extrapolation, direct comparison between oxide materials, or rapid iteration over wide ranges of temperature, material, and flow conditions for system-level performance optimization.

Most reactor designs can be conceptually categorized as fixedbed batch reactors, fluidized-bed batch reactors, or flow-through designs employing parallel-flow (PF), mixed flow, or countercurrent flow (CF) configurations. A general sketch of both PF and CF configurations is presented in Figure 1. Counter-current flow conditions are widely accepted as providing a theoretical upper limit on performance; however, as discussed by (Li et al., 2018b; Li et al., 2018a; Bulfin, 2019; de la Calle et al., 2022; and de la Calle et al., 2024), many past thermodynamic models for counter-current systems relied on inaccurate thermodynamic assumptions and thereby underestimate sweep gas and oxidizer flow requirements. This work aims to provide a simple thermodynamically-consistent model that can predict thermodynamic limits of O2 exchange in various systems of moving redox-active materials during reduction and oxidation, coupled with performance of system auxiliary units, in order to facilitate material comparison and wide-ranging evaluation of potential operating conditions.

The paper follows to detail the modeling framework (Section 2), demonstrate the use of the modeling framework through an analysis of redox systems for thermochemical $\rm H_2O$ and $\rm CO_2$ splitting (Section 3) as a sample use case, and ends with conclusions (Section 4).

2 Model

The thermodynamic model is based on the methodology developed and presented in (Bulfin, 2019), used in determining the thermodynamically-limited upper bounds of the process without considering transport limitations such as heat/mass transfer, or temperature and pressure gradients within the reactor system. We briefly present here the core methodology to allow

the reader to follow our additional development of model extensions. For the full derivation the reader is referred to the original paper by (Bulfin, 2019).

2.1 Original thermodynamic model and its application to thermal reduction

The problem is formulated using an exchange coordinate κ which is independent of the reactor size, as shown in Equation 4:

$$\kappa(x) = \frac{\int_0^x |\dot{j}_{\rm A}| \, \mathrm{d}x}{\dot{n}_1},\tag{4}$$

with A the species being exchanged, j_A as the molar flux of species A from flow 1 to flow 2, \dot{n}_1 as the molar flow rate of flow 1, and x the position along the reactor. In practical terms for redox cycles, κ would denote the change in the mole fraction of any reaction species along the reactor (an example provided in the Supplementary Material). The condition for a spontaneous transfer process of species A from flow 1 to flow 2 must fulfill Equation 5:

$$\mu_{A,1}(\kappa) \ge \mu_{A,2}(\kappa) \, \forall \kappa \in [0, \kappa_{\text{total}}],$$
(5)

with μ being the chemical potential. Applying the conservation of mass, we note that the number of moles of A that have left flow 1 must equal to the amount of moles that have entered flow 2, at any point along the reactor. For the parallel flow (co-current) case this yields in Equation 6:

$$\kappa_1 = \kappa_2 \equiv \kappa$$
(6)

while for counter-current flow the exchange coordinate of flow 2 is reversed, as shown in Equation 7 yielding

$$\kappa_1 = \kappa_2 - \kappa_{\text{total}} \equiv \kappa.$$
(7)

The thermodynamic upper limit for the exchange of A in a parallel flow (co-current) system is given by Equation 8:

$$\mu_{A,1}(\kappa_{\text{total}}) = \mu_{A,2}(\kappa_{\text{total}})$$
 (8)

with κ_{total} equal to κ at the reactor outlet. For the counter-current case, the chemical potential can meet at each boundary, share a common tangent somewhere within the reactor, or have all of species A transferred from flow 1 to flow 2. These are given by

$$\mu_{A,1}(0) = \mu_{A,2}(0) \text{ or } \mu_{A,1}(\kappa_{total}) = \mu_{A,2}(\kappa_{total})$$
 (9)

and

$$\frac{\partial \mu_{A,1}}{\partial \kappa} = \frac{\partial \mu_{A,2}}{\partial \kappa} \text{ and } \mu_{A,1}(\kappa) = \mu_{A,2}(\kappa)$$
 (10)

In the case of a complete transfer of A from flow 1 to flow 2, neither Equation 9 nor Equation 10 are binding, but the fundamental thermodynamic condition of Equation 5 is met within the entirety of the reactor length. Two system parameters that are needed to calculate the $\rm O_2$ exchange during reduction are the ratio between the molar flow rates of both streams Equation 11:

$$\omega_{\rm red} = \frac{\dot{n}_2}{\dot{n}_1} = \frac{\dot{n}_{\rm sg,in}}{\dot{n}_{\rm MO}},\tag{11}$$

and the O_2 mole fraction in the inert sweep gas $x_{O_2,in}$. $\dot{n}_{sg,in}$ is the molar flow rate of the inert sweep gas at the reactor inlet and \dot{n}_{MO} is the redox-active material molar flow rate. Assuming an isothermal and isobaric reactor, the chemical potential becomes a function of the O_2 partial pressure p_{O_2} . The O_2 partial pressure at the reactor outlet is then calculated as a function of κ . This can be obtained from the relation between the O_2 partial pressure and the O_2 mole fraction at the reactor outlet, after the oxygen exchange occurred Equation 12:

$$p_{\text{O}_2,\text{sg}}^{\text{red}}(\kappa) = \frac{x_{\text{O}_2,\text{in}}\omega_{\text{red}} + \kappa}{\omega_{\text{red}} + \kappa} p_{\text{red}}$$
 (12)

with $x_{O_2,in}$ as the O_2 mole fraction at the reactor inlet (function of the sweep gas purity), κ as the total O_2 exchange, and p_{red} as the total reactor pressure during reduction. Since each mole of O_2 released from the oxide will create two O vacancies in the oxide material, we can calculate the O_2 partial pressure of the oxide using Equation 13:

$$p_{\text{O}_{\alpha},\text{MO}}^{\text{red}}(\kappa) = f(T, \delta_{\text{ox}} + 2\kappa), \tag{13}$$

with $\delta_{\rm ox}$ as the initial non-stoichiometry extent at the end of oxidation and κ as the total O_2 exchange, same as in Equation 12. This formulation allows us to numerically solve for increasing κ from 0 to $\kappa_{\rm max}$, while checking the criteria in Equations 8–10 for each κ . The maximum O_2 transfer that is calculated without violating the constraints in Equations 8–10 is denoted as $\kappa_{\rm red}$, being the maximum species exchange during reduction.

2.2 Model extension

During the oxidation, a flow of H_2O or CO_2 enters the reactor and re-oxidizes the redox-active material, splitting the gaseous reactant into H_2 or CO, respectively. The conversion is usually incomplete, so the reactor outlet stream consists of a mixture of unconverted reactants and products. Following the same methodology as in the reduction reaction, we calculate the chemical potential of both gas and solid phases, to ensure the solution would adhere to requirements of a spontaneous process per Equation 5. The equilibrium constant for the thermolysis reaction (H_2O or H_2O) in the gas phase can be written as shown in Equation 14:

$$K = \frac{p_{\text{prod}} \left(\frac{p_{\text{O}_2}}{p^{\circ}}\right)^{\frac{1}{2}}}{p_{\text{reac}}} = \frac{x_{\text{prod}}}{x_{\text{reac}}} \left(\frac{p_{\text{O}_2}}{p^{\circ}}\right)^{\frac{1}{2}}$$
(14)

with the reactant and product mole fractions at the reactor effluent given by $x_{\rm reac} = \omega_{\rm ox} x_{\rm reac,in} - 2\kappa$ and $x_{\rm prod} = \omega_{\rm ox} x_{\rm prod,in} + 2\kappa$, respectively (and using $p_i = x_i p$). K is the relevant thermolysis reaction equilibrium constant (i.e., $H_2{\rm O}$ or ${\rm CO}_2$ thermolysis) and $\omega_{\rm ox}$ is the ratio between the molar flow rates of both streams during oxidation $\omega_{\rm ox} = \dot{n}_{\rm feed}/\dot{n}_{\rm MO}$ with $\dot{n}_{\rm feed}$ as the total feed molar flow rate which is given by $\dot{n}_{\rm feed} = \dot{n}_{\rm reac,in} + \dot{n}_{\rm prod,in}$. The equilibrium constant is calculated from $K = \exp\left(-\frac{\Delta G^0}{RT}\right)$. Substituting the partial pressure equations into Equation 14, assuming that $p_{\rm O_2} \ll p_{\rm reac}$ and $p_{\rm O_2} \ll p_{\rm prod}$, we can calculate the ${\rm O_2}$ partial pressure in the oxidizer stream using Equation 15:

$$p_{\text{O}_2,\text{feed}}^{\text{ox}}(\kappa) = p^{\circ} \left(K \frac{\omega_{\text{ox}} x_{\text{reac,in}} - 2\kappa}{\omega_{\text{ox}} x_{\text{prod,in}} + 2\kappa} \right)^2.$$
 (15)

The O_2 partial pressure of the oxide material is calculated via Equation 16:

$$p_{\text{O}_2,\text{MO}}^{\text{ox}}(\kappa) = f(T, \delta_{\text{red}} - 2\kappa)$$
 (16)

considering that this time the oxide is absorbing O_2 molecules from the oxidizer gaseous stream. By solving in the same manner as for the reduction, increasing κ from 0 to $\kappa_{\rm max}$, we can find the maximum O_2 exchange during the oxidation step $\kappa_{\rm ox}$ that satisfies the constraints in Equation 8, Equation 9, and Equation 10. Following the analysis of both steps, the maximum extent of re-oxidation (i.e., the lowest δ possible during oxidation at the reactor outlet) is calculated from Equation 17:

$$\delta_{\rm ox} = \delta_{\rm red} - 2\kappa_{\rm ox} \tag{17}$$

and the extent of reduction can be calculated as shown in Equation 18:

$$\Delta \delta = \delta_{\rm red} - \delta_{\rm ox} = 2\kappa_{\rm ox}.\tag{18}$$

Assuming full selectivity, the conversion of H₂O during water splitting oxidation can be calculated from Equation 19:

$$X = \frac{\dot{n}_{\text{prod,out}}}{\dot{n}_{\text{reac,in}}} = \frac{2\kappa_{\text{ox}}}{\omega_{\text{ox}}}$$
 (19)

with $\dot{n}_{\rm prod,out}$ as the product molar flow rate at the outlet (H₂ or CO) and $\dot{n}_{\rm reac,in}$ as the reactant molar flow rate into the reactor (H₂O or CO₂). Since conversion is limited to unity, the maximum value of κ during oxidation is $\kappa_{\rm max} = 0.5\omega_{\rm ox}$.

2.3 Redox thermodynamic formulation

To allow for a universal analysis of different redox materials, with different defect and vacancy formation mechanisms Zinkevich et al. (2006); Warren et al. (2022); Vieten et al. (2019); Wexler et al. (2023), we define the molar oxygen content fraction in the solid in Equation 20 as

$$\phi = \frac{n_{\rm O}}{n_{\rm MO}} \tag{20}$$

with $n_{\rm O}$ as the moles of O atoms in the solid and $n_{\rm MO}$ the moles of redox-active material solid. The amount of O atoms released during oxidation is then $\Delta\phi=\phi_{\rm ox}-\phi_{\rm red}$. In such a manner, we can use the same formulation for materials such as ceria and its solid solutions, perovskites, iron aluminates, and others. The relation between κ and ϕ is then given per Equation 21:

$$\phi_{\rm f} = \phi_{\rm i} \pm 2\kappa \tag{21}$$

with ϕ_f as the final state ϕ , ϕ_i as the initial state ϕ , and the sign dictated by the step, with minus for reduction (O atoms released from the solid) and plus for oxidation (O atoms absorbed by the solid). For materials with an oxygen vacancy mechanism, such as most redox-active materials studied to date (CeO₂ and its solid solutions, perovskites, and most ferrites), the total amount of oxygen exchanged in a cycle is equal in each formulation $\Delta \delta = \Delta \phi$. More details are provided in the Supplementary Material.

2.4 System performance

The connection between the thermodynamics of a specific redox-active material and its performance in the redox cycle to an actual system is based on a previously developed model Lidor and Bulfin (2024) and is aligned with other works in the field Bulfin et al. (2021). However, one generalization presented here is the clear separation of heat and work requirements. While it is customary to convert the auxiliary work to heat equivalent in the field of solar thermochemistry Bulfin et al. (2021), there is increased interest in hybrid CST-PV systems that would be able to provide both heat and power. Moreover, the emerging field of high-temperature electric thermal energy storage (ETES) Ma et al. (2023) opens up the possibility of using renewable electricity to drive the thermochemical reaction. Hence, we have excluded the energy conversion penalties associated with the energy input source, whether via solar thermal or other sources. Instead, we have calculated the overall thermochemical conversion process efficiency based on the required heat and power per

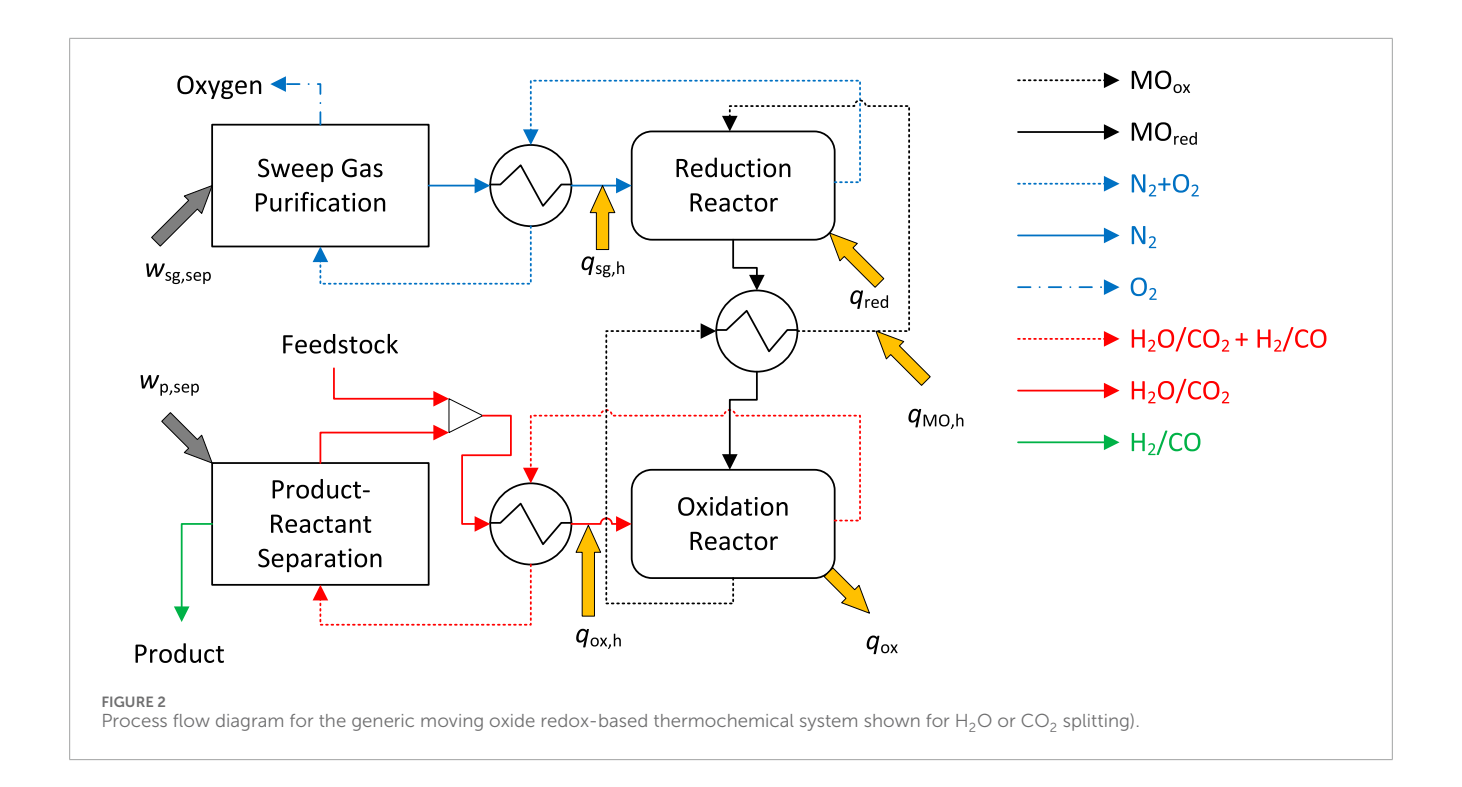
$$\eta = \frac{\dot{n}_{\text{fuel}} \text{HHV}_{\text{fuel}}}{\dot{Q}_{\text{req}} + \dot{W}_{\text{req}}},\tag{22}$$

with η as the efficiency, $\dot{n}_{\rm fuel}$ as the fuel production rate, HHV as the fuel higher heating value (upper limit of a fuel thermal energy, defined as the heat released during combustion assuming condensing of products that are liquid at the initial fuel temperature and pressure), $\dot{Q}_{\rm req}$ as the required thermal power, and $\dot{W}_{\rm req}$ as the required electric power for all necessary unit operations such as pumping and separation. Equation 22 can be divided by the flow rate of the redox-active material to be turned into a general form (not tied to a specific size/flow rate):

$$\eta = \frac{\Delta \phi \text{HHV}_{\text{fuel}}}{q_{\text{req}} + w_{\text{req}}},\tag{23}$$

with $\Delta\phi=\phi_{\rm ox}-\phi_{\rm red}$ as the specific amount of fuel produced per mole of redox-active material, $q_{\rm req}$ as the specific required heat per mole of redox-active material, and $w_{\rm req}$ as the specific required work per mole of redox-active material. From now on, we will use Equation 23 and the specific energy terms in this paper. The following energy terms are considered in this work:

- Sensible heating of the redox-active material between oxidation and reduction temperatures $(q_{MO,h})$.
- Heating of the inert sweep gas stream $(q_{sg,h})$.
- Heating of the oxidizer gas stream (q_{ox,h}), which can consist of both sensible and latent heat (in the case of water splitting). Even though the heat input in Figure 2 is presented between the sensible heat recovery and oxidation reactor, for the case of H₂O splitting, the required heat of vaporization to convert water into steam is of course supplied separately from the heat required to raise the steam temperature up to T_{ox}. For convenience we have lumped those into a single, general term, that is calculated accurately based on the oxidizer.
- Reduction energy (q_{red}) .
- Inert gas separation $(w_{sg,sep})$.
- Separation of product and unconverted reactant $(w_{p,sep})$.
- Exothermic heat of oxidation (q_{ox}). This term is not an energy input, but if recovered can be used to supply some of the heat



demand at $T < T_{ox}$, or used to provide heat for a power cycle that can cover some of the required work.

In addition, the effects of heat recovery, both in the gaseous streams (sweep gas and oxidizer gas) and in the solid stream, are evaluated by the implementation of heat recovery effectiveness values $\varepsilon_{\rm g}$ and $\varepsilon_{\rm s}$, respectively. This topic has been of great importance due to the large sensible energy needed for temperature-swing operation (Lidor et al., 2023; Patankar et al., 2022; Lidor and Zimmermann, 2023). It is also important for sweep gas operated systems which require large flow rates (Hathaway et al., 2016; Lidor et al., 2021). The possibility of recovering the exothermic heat of oxidation q_{ox} is also implemented in the same manner, using a heat recovery effectiveness ε_{ox} . This heat can be used to meet any heating requirements at temperatures below T_{ox} , such as oxidizer preheating or inert sweep gas heating to $T_{\rm ox}$. This heat can also drive an auxiliary power cycle that can be used to supply some of the required work. Since this model has been developed as a generic tool, capable of modeling a large variety of systems, the amount of usable exothermic heat is calculated assuming general heat recovery effectiveness, as well as heat-to-work efficiency in case this heat can cover all the thermal loads at or below $T_{\rm ox}$ and still has some excess. The full details of calculating each term are presented in the Supplementary Material.

The feedstock conversion extent is given by

$$X = 1 - \frac{\dot{n}_{\text{reac}}}{\dot{n}_{\text{reac,in}}} \tag{24}$$

with $\dot{n}_{\rm reac}$ as the unreacted feedstock molar flow rate at the effluent and $\dot{n}_{\rm reac,in}$ as the feedstock molar flow rate into the reactor. Since we perform an analysis normalized by moles of redox-active material, the conversion is calculated in our model from Equation 25:

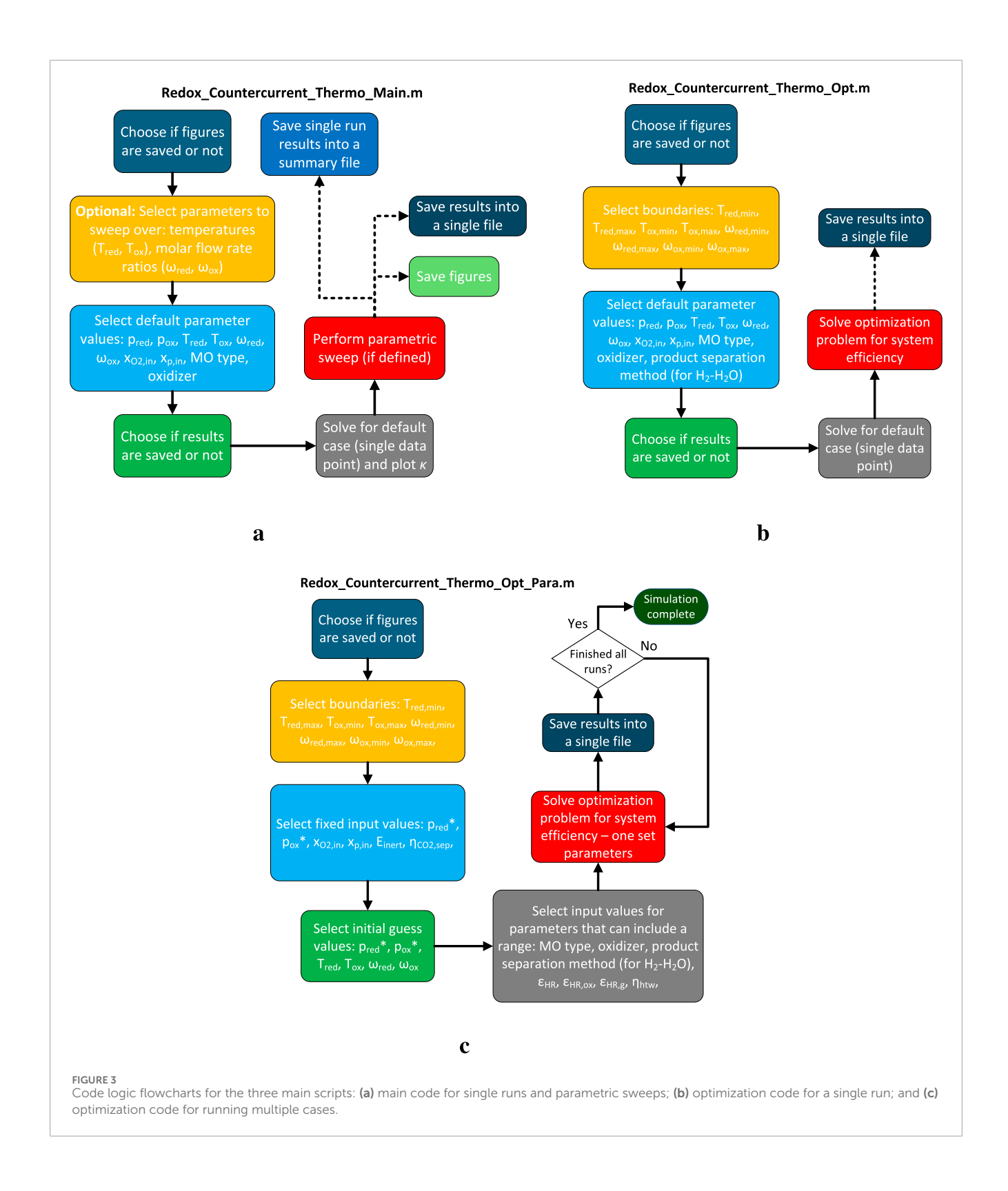
$$X = \frac{\Delta \phi}{\omega_{\text{ox}}} \tag{25}$$

which is in essence the moles of oxidizer that reacted per moles of redox-active material, over the moles of oxidizer fed into the reactor per moles of redox-active material.

2.5 Model structure

The model has been developed in MATLAB Version 2023b The MathWorks Inc. (2023) and is publicly available on a GitHub repository (https://github.com/NREL/REDOTHERM), including all the main scripts and required functions. The repository includes thermodynamic functions for several redox-active materials: CeO₂, $Ce_{0.8}Zr_{0.2}O_2$ (CeZr20), $La_{0.6}Ca_{0.4}Mn_{0.6}Al_{0.4}O_3$ (LCMA6464), $La_{0.6}Sr_{0.4}MnO_3$ (LSM40), and $Fe_{0.33}Al_{0.67}O_4$ (Fe33Al67). The thermodynamic data has been collected from (Bulfin et al., 2015; Bulfin et al., 2016; Carrillo and Scheffe, 2019; Warren et al., 2022), and uses either the provided functions for the reduction enthalpy $\Delta h_{\text{red}}(\delta)$ and reduction entropy $\Delta s_{\text{red}}(\delta)$ (Bulfin et al., 2015; Bulfin et al., 2016) or uses a curve fitting tool to develop polynomial correlations from the given data (Carrillo and Scheffe, 2019; Warren et al., 2022). We note that when using curve fitting methods to calculate the material thermodynamic properties, a certain degree of inaccuracy is expected, especially if the original experimental data is limited in terms of temperature and δ . Extrapolating beyond the range of the material data can be unreliable, and care should be taken in interpreting results from the sensitivity analysis and optimization capabilities described below when conditions extend beyond the limits of the measured material performance.

Thermodynamic properties of the fluids in the system are calculated using the CoolProp package (Bell et al., 2014) at the relevant process temperature and pressure, and the equilibrium composition of the oxidizer feed is calculated using the Gibbs energy



minimization method implemented with Goodwin et al. (2023). The oxidizer gas can be selected as either $\rm H_2O$ or $\rm CO_2$, as the necessary equilibrium constant calculation is performed for the relevant thermolysis reaction, based on the oxidizer feed of each analysis. The model is developed with an interactive input acquisition (via

prompts) for the main parameters which are expected to be changed frequently, such as temperatures, and other parameters which are set within the code. There are three main scripts that are to be used when running the model with their respective code logic flowcharts in Figure 3:

TABLE 1 Overview of the different options of the REDOTHERM code.

System parameter	Options
Redox-active material	CeO ₂ , CeZr20, LCMA6464, LSM40, Fe33Al67
Oxidizer type	H ₂ O, CO ₂
${ m H_2O-H_2}$ separation method	Condensation, mechanical vapor recompression
CO ₂ –CO separation method	Pressure swing adsorption
Heat recovery options	Sensible solid, sensible gas, oxidation heat
Decision variables for parametric sweeps/optimization ^a	$T_{\mathrm{red}}, T_{\mathrm{ox}}, p_{\mathrm{red}}, p_{\mathrm{ox}}, \omega_{\mathrm{red}}, \omega_{\mathrm{ox}}$

 $^ap_{\rm red}$ and $p_{\rm ox}$ are passed as decision variables but currently constrained to be equal to a single value.

- Main code: Redox_Countercurrent_Thermo_Main.m this script is used to solve for a single data point (i.e., one combination of temperatures, pressures, molar flow rate ratios, etc.) and obtain the redox performance in terms of $\Delta\delta$, $\Delta\phi$, and X. It can also be used to perform parametric sweeps over combinations of $T_{\rm red}$ and $T_{\rm ox}$ and/or $\omega_{\rm red}$ and $\omega_{\rm ox}$. The results can be saved in a file that can be post-processed for cycle performance and plotting via the support script Redox_Countercurrent_Thermo_Plot_Results.m. The logic flowchart of this script is presented in Figure 3a.
- Optimization code: $Redox_Countercurrent_Thermo_Opt.m$ this script is used to run an optimization analysis, aimed at identifying the operating conditions in terms of $T_{\rm red}$, $T_{\rm ox}$, $\omega_{\rm red}$, and $\omega_{\rm ox}$ which will yield the highest system efficiency η . The code does not have any built-in plotting, but will display the results and include optional saving of the data to a MAT file. The logic flowchart of this script is presented in Figure 3b.
- Optimization code with parametric sweeps: $Redox_Countercurrent_Thermo_Opt_Para.m$ this script is used to automate multiple optimization analysis runs, facilitating sweeps over different redox-active materials, heat recovery effectiveness values $(\varepsilon_s, \varepsilon_{ox}, \varepsilon_g)$, heat-to-work efficiency (η_{htw}) , oxidizer type, and product separation method (for H_2-H_2O). The script automatically saves each run with a set of parameters to a MAT file. No plotting or results display capabilities are currently included; however, a simple plotting script $Plot_multiple_opt_results.m$ used in generating plots for this paper is provided in the repository and can easily be extended for different types of data analysis. The logic flowchart of this script is presented in Figure 3c.

The reactor pressures during reduction (p_{red}) and oxidation (p_{ox}) are passed to the optimization problem as decision variables, but are currently fixed via constraints/bounds (depending on the optimizer used). The motivation behind this is two-fold: (1) to allow the analysis of hybrid vacuum-sweep gas systems, which requires both inert sweep gas separation as well as vacuum pumping work terms; (2) to allow future inclusion of any downstream pumping requirements, which in turn might promote the use of high pressure

oxidation due to the benefits of pumping water, and obtaining high-pressure $\rm H_2$ for storage or downstream processes such as Fischer-Tropsch.

Cryogenic separation was selected for inert gas separation. Pressure swing adsorption (PSA) was implemented for product separation for CO₂, while H₂O splitting includes options for conventional condensation and evaporation of the make-up feed and condensed water, as well as a mechanical vapor recompression (MVR) cycle separation which can recover the latent heat (based on Lidor, 2024).

All the different options for the REDOTHERM code are provided in Table 1. The full details of the calculation methods for each term are given in the Supplementary Material.

3 Results

The basic capability of the model in predicting the redox performance of a water-splitting cycle is demonstrated for the case of CeO₂. In Figure 4a the maximum O₂ exchange is presented for reduction at $T_{\rm red}$ = 1,550 °C using an inert sweep gas with O_2 mole fraction $x_{O_2,in} = 10^{-4}$ and molar flow rate ratio $\omega_{red} = 1$ for both PF and CF configurations. As expected, the maximum O2 exchange κ is larger for CF than for PF, with the resulting $\delta_{\rm red}$ of 0.032 and 0.0203 and $\Delta\delta$ (identical to $\Delta\phi$ for the case of CeO₂) of 0.0286 and 0.0176, respectively. While the values slightly differ from those presented in (Bulfin, 2019) for an identical case, the source of the difference has been identified as the selection of a different function for the redox thermodynamics of CeO2. We compare four different correlations for $p_{O_2}(T, \delta)$ of CeO_2 : (1) a general calculation of p_{O_2} based on equilibrium thermodynamics (see Supplementary Material) combined with piecewise fitting of the Panlener $\Delta h_{\rm red}(\delta)$ and $\Delta s_{\rm red}(\delta)$ data (Panlener et al., 1975) which has been implemented in this work; (2) a defect model derived using statistical physics from (Bulfin et al., 2016); (3) a constant ΔH model used in (Bulfin et al., 2016); and (4) a correlation by (Ackermann et al., 2017) extracted from the data of (Panlener et al., 1975). As a reference, we also provide the raw data from (Panlener et al., 1975). The results of this comparison are presented in Figure 5. It is clear that in the region of $\delta \le 0.05$, which is the most relevant for our application, there are minor differences between these models and these differences significantly increase for some models when $\delta \ge 0.05$. These differences cause the deviation in the prediction of the O2 exchange. This also emphasizes the importance of accurate thermodynamic properties modeling and data (Wilson et al., 2024) over a wide range of compositions as well as extraction from experimental results (Lany, 2024).

3.1 Parametric sweep capability

The parametric sweeps that are implemented in the main code ($Redox_Countercurrent_Thermo_Main.m$) are useful in investigating the effects of different operation and design parameters on all the different energy terms of the system as well as on its performance indicators. We present as an example the results of a parametric sweep over the molar flow rate ratios $\omega_{\rm red}$ and $\omega_{\rm ox}$ for CeO₂ for a case of H₂O splitting. The temperatures are set at

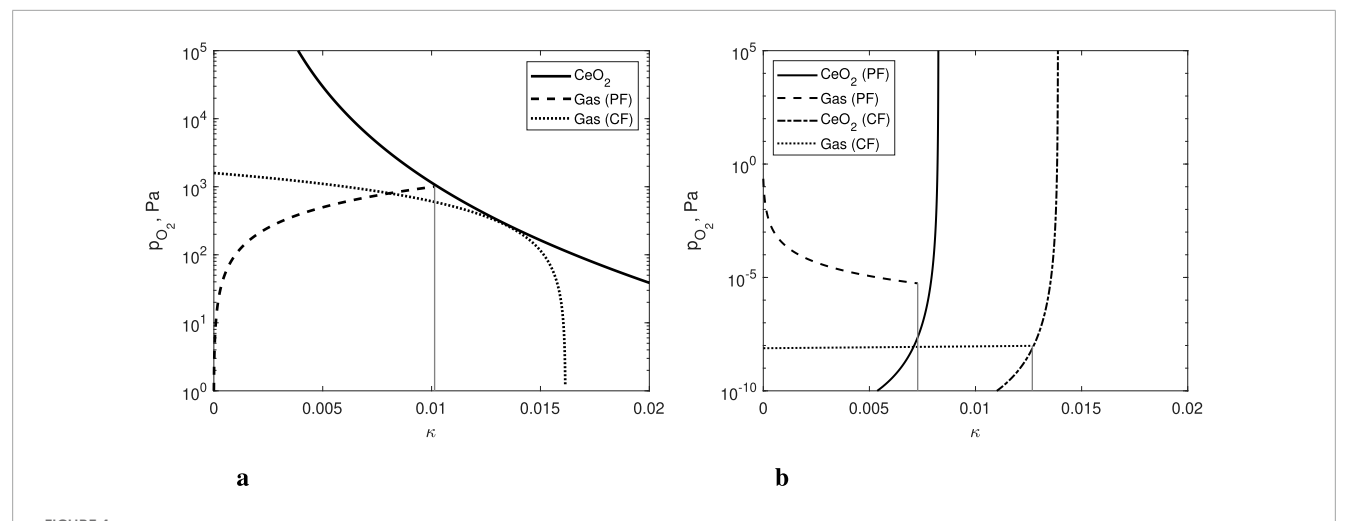
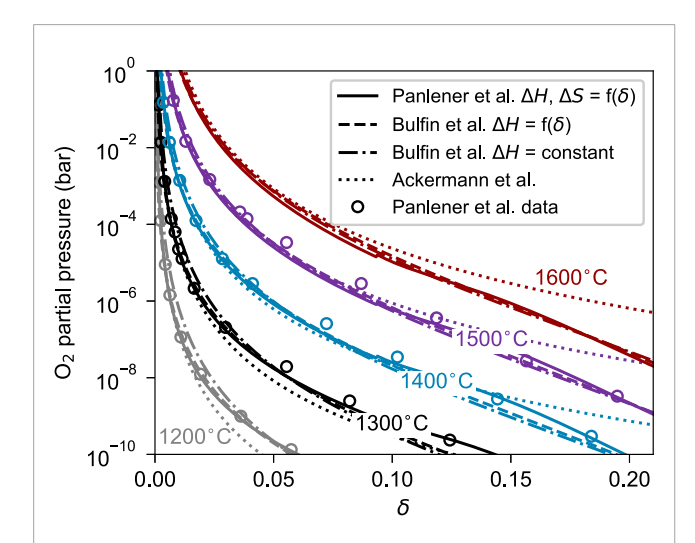


FIGURE 4
The O₂ partial pressure p_{O_2} as a function of the exchange coordinate κ for the PF and CF cases with CeO₂: (a) reduction at $T_{\text{red}} = 1550$ °C, $X_{O_2,\text{in}} = 10^{-4}$, and $\omega_{\text{red}} = 1$; and (b) oxidation with H₂O at $T_{\text{ox}} = 900$ °C, $\omega_{\text{ox}} = 1$, and $X_{\text{H}_2,\text{in}} = 4.8 \cdot 10^{-6}$ (equilibrium H₂ mole fraction at inlet conditions).



Comparison of the oxygen partial pressure $p_{\rm O_2}$ of CeO₂ based on four different correlations: (1) general equilibrium thermodynamics using piece-wise fit of the data from Panlener et al. (1975) (2) defect model from Bulfin et al. (2016) with reduction enthalpy as a function of δ ; (3) defect model from Bulfin et al. (2016) with constant reduction enthalpy; and (4) correlation of the data from Panlener et al. (1975) from Ackermann et al. (2017). The circles denote original data from Panlener et al. (1975).

 $T_{\rm red}=1550~{\rm ^{\circ}C}$ and $T_{\rm ox}=900~{\rm ^{\circ}C}$. The inert sweep gas purity is $x_{\rm O_2,in}=10^{-5}$, and equilibrium $\rm H_2$ mole fraction at inlet conditions is assumed ($x_{\rm H_2,in}=4.8\cdot10^{-6}$). The $\rm H_2-H_2O$ separation method selected is MVR, and while the code analyzes the performance of both PF-PF and CF-CF configurations, we are presenting here only the CF-CF case for brevity. The trade-off between obtaining a higher $\Delta\delta$ at the expense of conversion using higher gas molar flow rates (i.e., higher $\omega_{\rm red}$ and $\omega_{\rm ox}$) is clearly demonstrated in Figure 6. The regions which exhibit a value of X>0.1, which has been referred to in different studies (Bayon et al., 2022; Lidor and Bulfin, 2024) as the

minimum viable conversion extent, barely overlaps with the areas of high $\Delta\delta$. Of course, this set of plots do not reveal the complete picture: having a $\Delta\delta$ that is too low would reduce the efficiency since a small amount of fuel is produced.

We also calculate the system efficiency for these parametric sweep cases. The values used for the various heat recovery unit operations are $\varepsilon_s = 0.5$, $\varepsilon_g = 0.8$, and $\varepsilon_{ox} = 0.8$. The rest of the terms used in the calculation of the system efficiency, including specific energy and efficiency terms for some of the auxiliary units, are provided in the Supplementary Material. The results of the cycle efficiency analysis are presented in Figure 7 for the same sample case, using two types of product separation, conventional steam condensation (Figure 7a) and MVR-based separation (Figure 7b). A maximum efficiency of 11.2% and 13.93% is identified for condensation and MVR-based system, respectively. We note the low values compared to other predicted values from the literature. This is due to the following reasons: (a) we do not attempt to optimize the system in this example, except for the two parameters swept ($\omega_{\rm red}$ and ω_{ox}); (b) some of our system parameter assumptions, such as heat recovery effectiveness, are more modest than other studies; (c) our analysis includes the correct thermodynamics limits, which are not implemented in most studies; and (d) we have accounted for the separation and steam generation energy terms, which are often neglected.

By examining the rest of the performance maps for the different energy fraction terms (sensible heating, etc.), one can obtain important insights into the specific thermochemical hydrogen (TCH) process that is evaluated, both from material and system perspective. The plots for this analysis are provided in the Supplementary Material.

3.2 Optimization capability

The optimization capability of the REDOTHERM code includes a single case optimization, as well as optimization for multiple cases, in which the model sweeps over a range of values for the

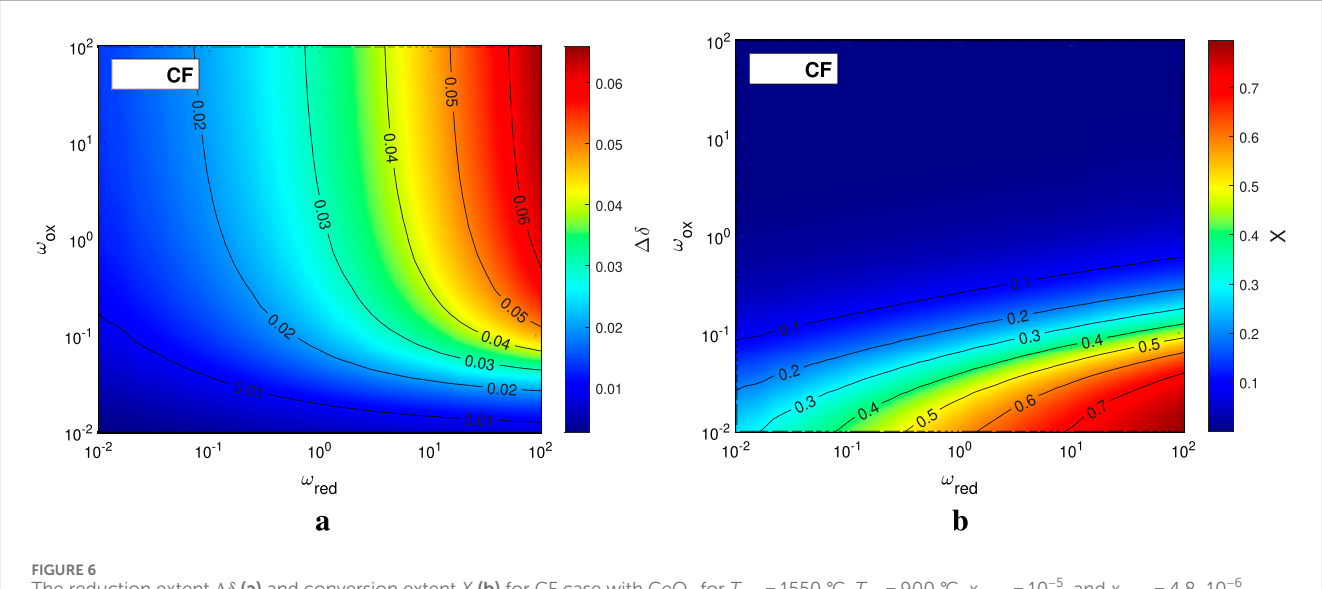
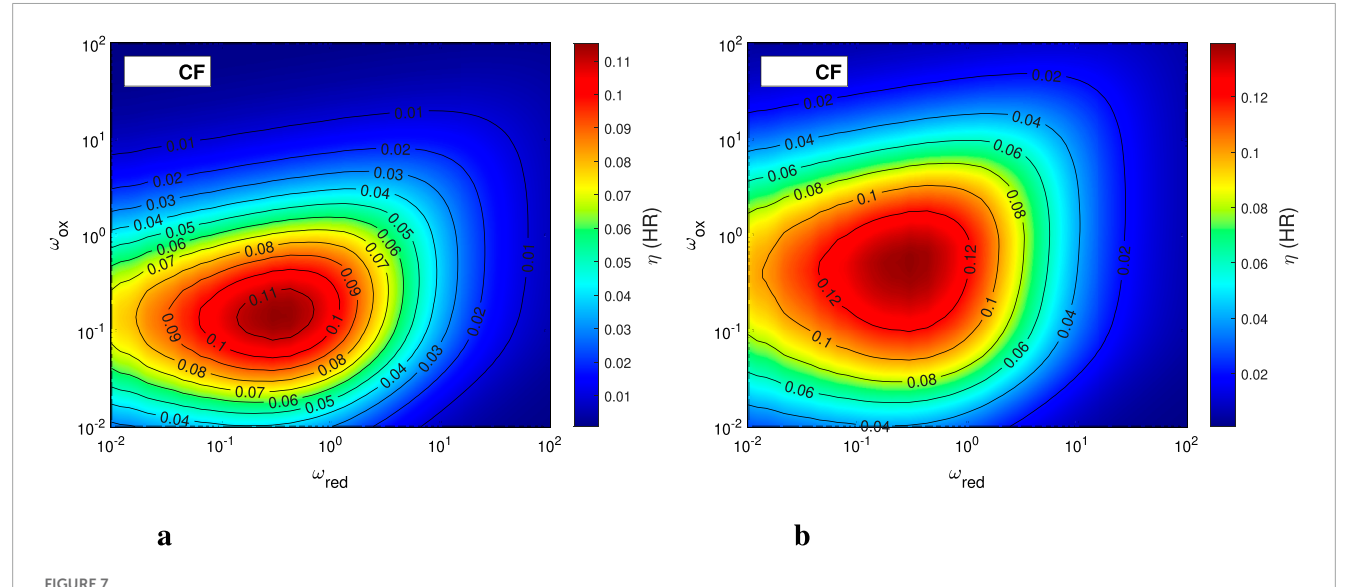


FIGURE 6
The reduction extent $\Delta\delta$ (a) and conversion extent X (b) for CF case with CeO_2 for $T_{red} = 1550$ °C, $T_{ox} = 900$ °C, $X_{O_2,in} = 10^{-5}$, and $X_{H_2,in} = 4.8 \cdot 10^{-6}$ (equilibrium H_2 mole fraction at inlet conditions).



The cycle efficiency for CF case with CeO₂ for $T_{\rm red}$ = 1550 °C, $T_{\rm ox}$ = 900 °C, $x_{\rm O_2,in}$ = 10⁻⁵, and $x_{\rm H_2,in}$ = 4.8 · 10⁻⁶ (equilibrium H₂ mole fraction at inlet conditions). H₂–H₂O separation method: (a) condensing the effluent after sensible heat recovery; (b) using MVR-based separation cycle to recover the latent heat.

different system parameters, such as redox-active material type, heat recovery effectiveness, and so forth. A sample usage is given here, demonstrating how it can be used to compare different redox-active materials, under the same operating conditions and boundaries. The input parameters, as well as the ranges of the decision variables, are given in Table 2. The optimization problem is solved using a direct search method (*patternsearch* in MATLAB) with the Nonuniform Pattern Search (NUPS) algorithm.

Five values for ε_s from 0 to 1 were included, examining all cases under both extremes, with no solid heat recovery up to an ideal (and nonphysical) full solid heat recovery. The analysis is performed for water splitting cycles and includes both

condensation with reboiling and MVR as the product separation options. The analysis is demonstrated for atmospheric reduction (with sweep gas) and oxidation; however, the option to perform either step at different pressures is included as well. Performing the oxidation at elevated pressures can benefit from increased $p_{\rm O_2}$ in the oxidizer stream, which can increase the extent of reoxidation (Tran et al., 2023). However, the major improvement is achieved from obtaining the produced H_2 at pressure, thus saving on the costly compression that is needed for any produced hydrogen. Lastly, we assume no thermal losses from the reactor ($f_{\rm th,loss}=0$), since this analysis is performed for a generic moving oxide system without a specific reactor design.

TABLE 2 Input parameters and ranges for decision variables for the REDOTHERM optimization analysis.

System parameter	Options
Redox-active material	CeO ₂ , CeZr20, LCMA6464, LSM40, Fe33Al67
Oxidizer type	H ₂ O
H ₂ O-H ₂ separation method	Condensation, MVR
Solid heat recovery effectiveness $\varepsilon_{\rm s}$	0, 0.25, 0.5, 0.75, 1
Gas heat recovery effectiveness $arepsilon_{ m g}$	0.8
Oxidation heat recovery effectiveness $\varepsilon_{\rm ox}$	0.4, 0.8
Thermal losses fraction $f_{\mathrm{th,loss}}$	0
Inert sweep gas purity $x_{O_2,in}$	10 ⁻⁵
Oxidizer purity $x_{\text{ox,in}}$	0.99999
Reduction pressure $p_{\rm red}$	1 bar
Oxidation pressure p_{ox}	1 bar
Reduction temperature $T_{\rm red}$	[1400 °C,1700 °C]
Oxidation temperature $T_{\rm ox}$	[600 °C,1200 °C]
Sweep gas to oxide molar flow rate ratio $\omega_{\rm red}$	[0.001,1000]
Oxidizer to oxide molar flow rate ratio ω_{ox}	[0.001,1000]

The summary of the results from the optimization run is presented in Figure 8. We focus on a baseline case with $\varepsilon_s=0.5$, an extreme case of no solid heat recovery $(\varepsilon_s=0)$ and an ideal full solid heat recovery $(\varepsilon_s=1)$. In all of those cases the oxidation heat recovery was taken as $\varepsilon_{\rm ox}=0.8$. Note that the optimization in Figure 8 considers a wide range of reduction and oxidation temperature conditions, and extends beyond the range of available oxide material thermodynamic data in some cases. We present these results to demonstrate the capabilities of the model, but caution that results from the optimization should ideally be combined with sensitivity analyses to understand the behavior in the vicinity of the optimum and to verify that the material thermodynamic performance is reasonable within this region of the parameter space.

In Figure 8a we can see that the efficiency of ${\rm CeO_2}$ is higher than all other materials. When considering the reduction enthalpy of the different materials, a clear trend is observed that materials with higher values of the enthalpy of oxygen vacancy formation exhibit higher efficiency values. As expected, the reduction temperature in all the optimal solutions converged to the upper bound (1700 °C), with less than 10 °C below this limit in all 80 solutions. This trend is identical to the results reported in (Li et al., 2018a). It implies the model can be modified to provide $T_{\rm red}$ as an input,

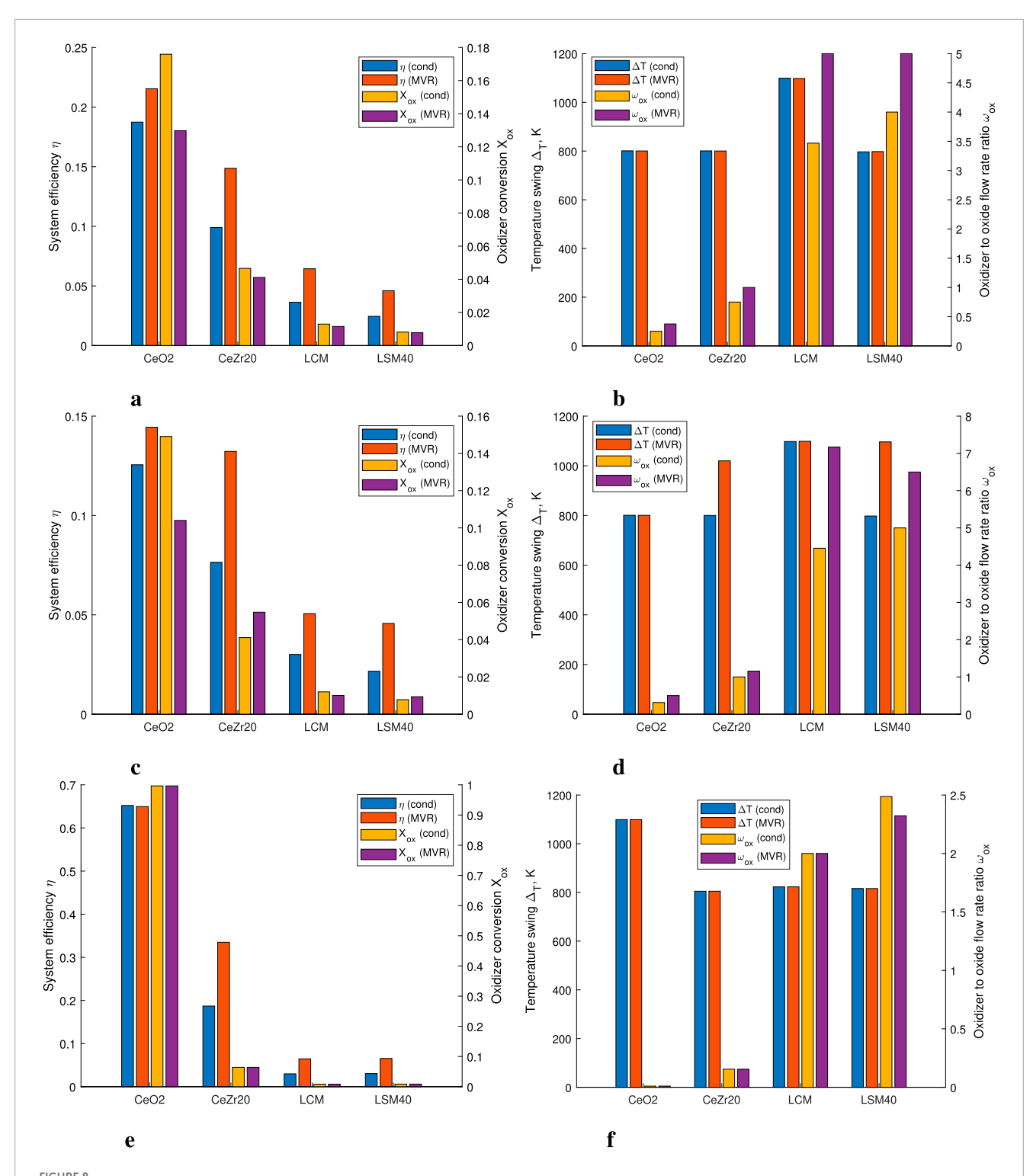
thus removing one decision variable from the optimization space, potentially lowering the required computational load. However, the temperature swing varied as can be seen from Figure 8b, with most materials converging to an optimal solution with $\Delta T = 800$ °C while LCMA6464 benefitting from a large value of ΔT . When examining Figure 8f, one would expect that all materials will converge to the maximum ΔT possible since having a temperature swing does not require any sensible heating when $\varepsilon_s = 1$. However, we see that only CeO_2 exhibits the largest ΔT possible. While not included here for brevity, our hypothesis why materials with lower reduction enthalpies, that would benefit from a larger temperature swing, are limited in their ΔT is due to the high requirements of sensible heating of the oxidizer stream, that still has a value of $\varepsilon_g = 0.8$. This type of investigation, deeply examining all the intricate effects of the different system components and their effects on the performance for different redox materials, is what we envision REDOTHERM most suitable for. Another important finding is that CeO2 and CeZr20 are the only materials that have a value of $\omega_{\rm ox}$ below 1; all other materials require excessive amounts of steam for reoxidation, with up to $\omega_{ox} = 14$. While known in the literature (Bayon et al., 2022; Lidor and Bulfin, 2024), this side-by-side comparison highlights the importance of examining all operating parameters and design considerations when comparing different redox-active materials.

Examining a specific subset of results, we present in Figure 9 the specific energy terms for each of the evaluated redox-active materials for the base case optimized solution (i.e., $\varepsilon_s = 0.5$ and $\varepsilon_{\rm ox} = 0.8$). The energy terms are normalized by the amount of produced H₂. When examining the case of using condensation as the H₂-H₂O separation method (Figure 9a), it can be seen that for CeO₂ and CeZr20 the specific reduction energy and specific sensible MO required heating are the dominant factors (with CeO₂ as the only case when the specific reduction energy is the largest term), while for the other materials the required heat for steam generation is dominant (the required product separation work is zero, since the load is only thermal). This supports the findings presented in Figure 8, with an inverse correlation between the ease of reduction (via the reduction enthalpy) and the performance. For the case of using MVR separation (Figure 9b) the value of the required sensible MO heat is the dominant factor across all the materials, except CeO₂ in which it is the second largest term, following the specific reduction energy (identical to the condensation case for CeO₂).

The example cases shown in this section provide a brief overview of the capabilities of REDOTHERM. Extending upon them for new redox-active materials, both real and hypothetical, as well as adding more technology options for the auxiliary operations, is relatively straightforward and could support the field in the search for efficient and scalable designs.

3.3 Example of usage

In this subsection, we demonstrate the use of the REDOTHERM repository in a few types of analysis that can benefit different research activities within the TCH and chemical looping redox fields.



Comparison of the system efficiency, oxidizer conversion extent, temperature swing, and oxidizer to metal oxide flow rates ratio for different redox materials, using both condensation with reboiling and MVR as the H_2 - H_2 O separation methods. All values are for the optimal solution (optimized for η). (a) Baseline case: η , X. (b) Baseline case: ΔT , ω_{ox} . (c) No solid HR case: η , X. (d) No solid HR case: ΔT , ω_{ox} . (e) Full solid HR case: η , X. (f) Full solid HR case: ΔT , ω_{ox} .

3.3.1 Productivity compared to efficiency and conversion

Many papers that deal with the discovery and characterization of TCH materials use the productivity (or yield) as the benchmarking

performance indicator, defined as the amount of generated gaseous product (O_2 for the reduction step and H_2 or CO for the oxidation step) over the mass of the oxide sample, usually given in μ mol g⁻¹ (Hao et al., 2014; Yang et al., 2014; Warren et al., 2022;

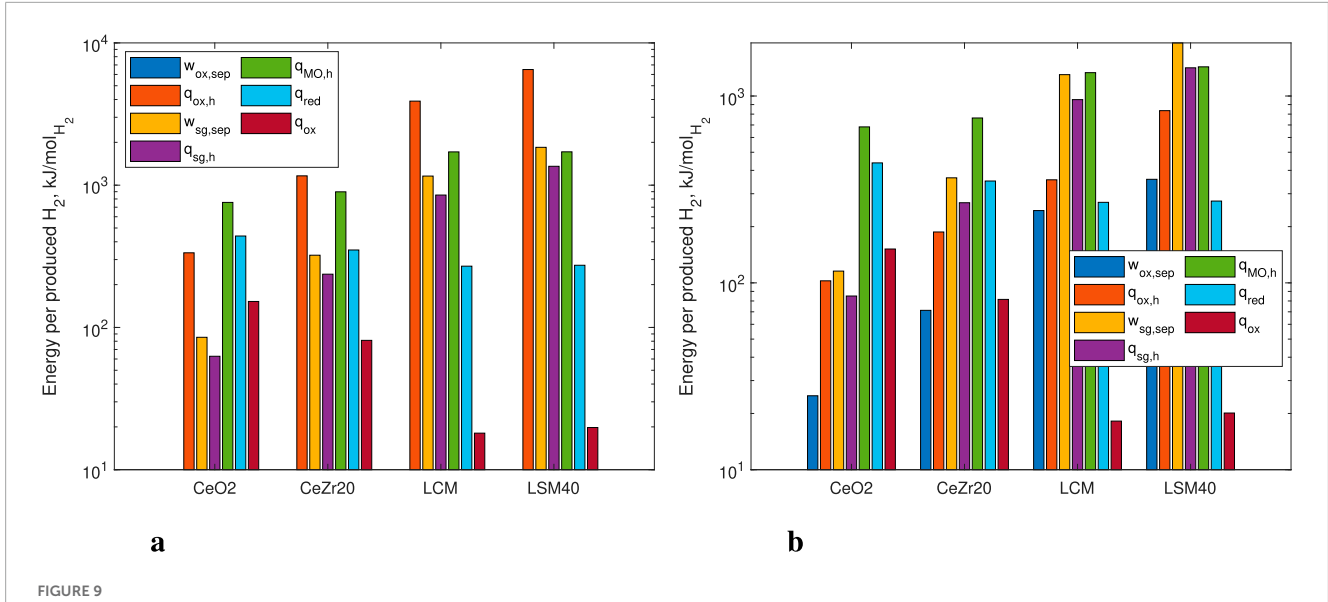


FIGURE 9
Energy terms for different redox-active materials normalized per mole of produced H₂. (a) H₂-H₂O separation using condensation, and (b) H₂-H₂O separation using MVR. All values are for the optimized solution using base case parameters: $\varepsilon_s = 0.5$, $\varepsilon_{ox} = 0.8$.

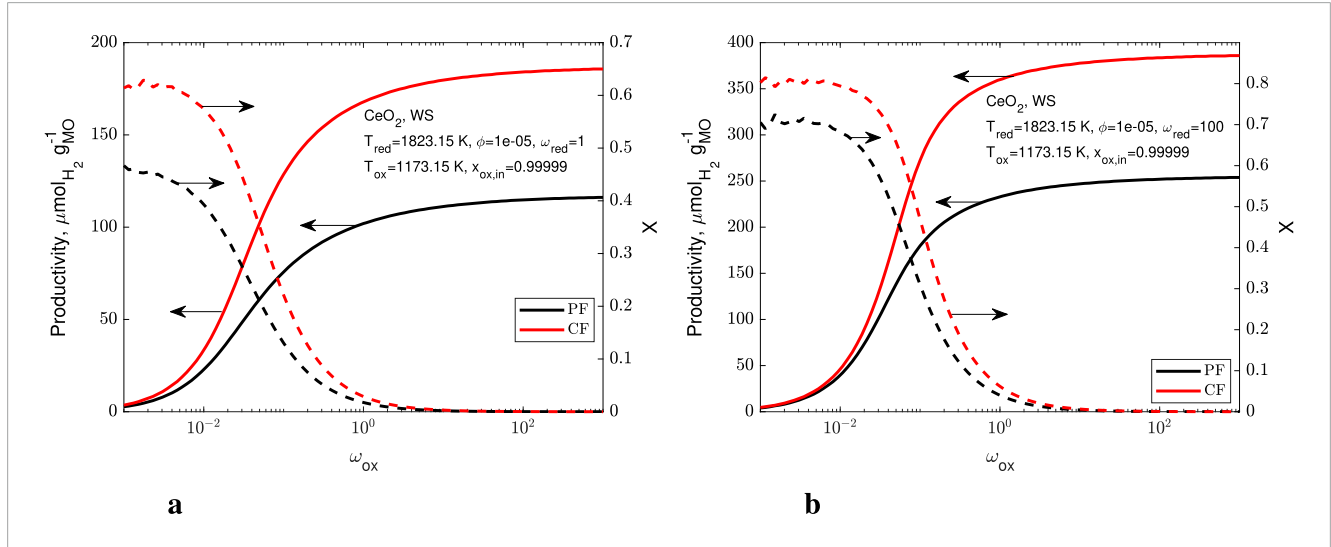
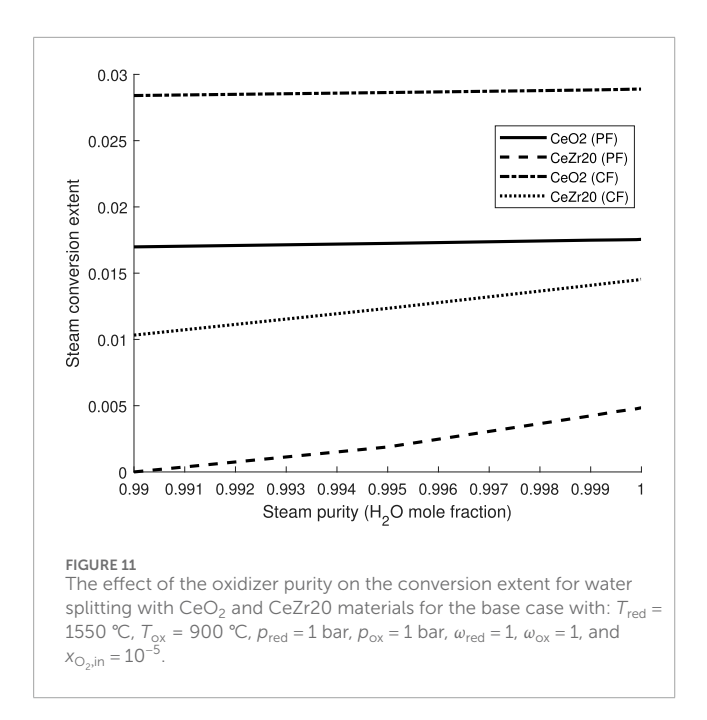


FIGURE 10 Productivity (solid lines) and conversion extent (dashed lines) as a function of the ratio of the oxidizer molar flow rate to the redox-active material molar flow rate for CeO_2 undergoing a water splitting cycle. (a) Oxidation step following reduction with $\omega_{red} = 1$, and (b) oxidation step following reduction with $\omega_{red} = 100$. Parameters used are $T_{red} = 1550$ °C, $T_{ox} = 900$ °C, $T_{ox} = 100$, and $T_{ox} = 100$ oxidation step following reduction with $T_{ox} = 100$ oxida

McCord et al., 2024). While useful for comparing different redoxactive materials under identical conditions, this performance indicator is insufficient by itself to properly inform on the potential of a redox-active material and its comparison to other materials, especially under industrially-relevant process conditions. Most redox-active material characterization is performed using a thermogravimetric analyzer (TGA) or stagnation flow reactor (SFR), under conditions which supply a large excess of an inert gas during reduction and a large excess of oxidizer gas (at a controlled partial pressure) during oxidation. Hence, the obtained productivity should be treated as an ideal upper limit, since providing inert sweep gas or oxidizer in large excess can have a significant

negative effect on the overall system efficiency (Equation 22) and conversion (Equation 24).

In Figure 10 we present the productivity and conversion extent for CeO_2 undergoing a water splitting redox cycle as a function of the oxidizer to redox-active material molar flow rates ratio ω_{ox} . In Figure 10a the results are presented for a case in which the reduction was performed under $\omega_{\text{red}} = 1$, simulating a case of industrially-relevant conditions, avoiding extreme excess of inert sweep gas which would require extremely large separation energy. It can be seen that under these conditions, even when supplying excess oxidizer at high purities, the productivity is lower than reported for CeO_2 (Warren et al., 2022; McCord et al., 2024). More importantly



is the clear trade-off that is exhibited between productivity and conversion extent; values of $X \ge 0.1$ are not possible for $\omega_{ox} > 0.2$. The importance of the conversion extent and the need to reach a minimal realistic value is discussed elsewhere (Bayon et al., 2022; Lidor and Bulfin, 2024). For comparison, Figure 10b presents the productivity and conversion extent as a function of ω_{ox} for a case in which the reduction was performed with a great excess of inert sweep gas ($\omega_{\rm red}$). As expected, the productivity increases significantly, by about a factor of 3-4 under similar values of $\omega_{\rm ox}$. However, achieving $X \ge 0.1$ is only possible for $\omega_{\rm ox} \le 0.4$, which is not a significant improvement compared to the case with lower excess sweep gas. We note the small artifacts occurring for the CF case when ω_{ox} approaches 0.001 - these are a result of numerical instabilities, which would require refining the steps of κ to resolve, significantly increasing the computational time. This analysis shows the limitations of using productivity as the sole performance indicator that guides material discovery. Since productivity is missing kinetic effects (cycle duration) and is often not evaluated under industrially-relevant conditions (gas to oxide flow rate ratios), materials that exhibit high productivity might actually underperform compared to materials which seem less promising based on this sole criteria.

In the same manner, REDOTHERM can be used to quickly evaluate the effects of the oxidizer purity on the redox performance. While in theory a feed of pure steam (or CO₂) is preferred, the relatively limited conversion of the oxidation reaction necessitates the recycling of the unreacted oxidizer gas, after separation from the product (H₂ or CO). Depending on the separation technology, some trace product will be left in the oxidizer stream. The effects of this recycled product on the oxidizer conversion extent are presented in Figure 11. The analysis is performed for our base case scenario with $T_{\rm red}=1550$ °C, $T_{\rm ox}=900$ °C, $p_{\rm red}=1$ bar, $p_{\rm ox}=1$ bar, $\omega_{\rm red}=1$, $\omega_{\rm ox}=1$, and $x_{\rm O_2,in}=10^{-5}$.

From these results, we can see that CeO₂ is insensitive to higher impurities, and exhibits almost constant conversion, while CeZr20

shows some decrease in the conversion as the purity drops. It is expected that other materials with lower reduction enthalpies will exhibit even larger sensitivities to oxidizer gas impurities. This type of analysis can be used to determine realistic purity requirements for different redox-active materials.

3.3.2 Implementation for system and technoeconomic analysis of a specific case study

While all the performance indicators and results calculated by REDOTHERM are either dimensionless or specific values (per mole of redox-active material), the conversion to explicit values for a specific case study is straightforward. The use of REDOTHERM to size up a process for a given $\rm H_2$ production capacity $\dot{m}_{\rm H_2}$ starts by converting the production capacity (usually in t d⁻¹) to a molar production capacity $\dot{n}_{\rm H_2}$. The required steam molar flow rate is then given by Equation 26:

$$\dot{n}_{\rm H_2O,in} = \frac{\dot{n}_{\rm H_2}}{x_{\rm H_2,in} + X},\tag{26}$$

with $x_{\rm H_2,in}$ as the H₂ mole fraction at the feed (trace H₂ that remains after product separation). Assuming that $x_{\rm H_2,in} \ll 1$, the difference between the total molar flow rate of the feed $\dot{n}_{\rm feed}$ and $\dot{n}_{\rm H_2O,in}$ is negligible. The required flow rate of the redox-active material is then calculated from Equation 27:

$$\dot{n}_{\rm MO} = \frac{\dot{n}_{\rm H_2O,in}}{\omega_{\rm ox}}.$$
 (27)

All the specific energy terms q_i and w_i can then be used to calculate the required power or heat using Equation 28:

$$\dot{Q}_{i} = q_{i} \dot{n}_{MO} \tag{28}$$

with i as the index specifying which term (i.e., inert gas separation, solid sensible heating, e.g.). From this, it is straightforward to perform sizing calculations for the auxiliary units, as well as sizing up the energy source, whether using CST or other. It can also be coupled to a hydrogen production financial model, such as ProFAST, to obtain a physics-based TEA framework (Kee and Peney, 2023).

4 Conclusion

The developed REDOTHERM model provides a comprehensive basis for analysis of different redox-based chemical looping systems for a variety of applications, with the initial focus on thermochemical hydrogen and syngas production. REDOTHERM is an open-source tool that can be used as a benchmarking tool for research and development work in this field. REDOTHERM can benefit the following activities:

- Material discovery efforts: through quick prediction of the effects of design parameters on expected system performance, researchers could screen potential materials more efficiently, as well as couple system performance considerations to computational chemistry frameworks for designing materials with specific desired properties.
- 2. Reactor and system modeling: using REDOTHERM could allow reactor and system development efforts to quickly

identify upper bound performance. While the model lacks detailed transport phenomena modeling, if the predicted performance for a system using REDOTHERM falls short of the target efficiency, an actual reactor/system would be unable to meet it.

3. Technoeconomic analysis (TEA): many TEA studies follow a simple 'figure-of-merit' approach, in which performance of different unit operations is assumed to meet a given value. While reasonable for established technologies with long operational data, when used for low technology readiness level (TRL) technologies such as redox-based chemical looping, there is not always a justification for selecting specific values. REDOTHERM could be coupled with a TEA framework to improve cost predictions and help in understanding the effects of different design and operating conditions on the cost of the product.

Natural future extensions and additions to REDOTHERM capabilities include adding models for the upstream energy generation, whether through solar thermal or other sources; including more auxiliary technology options; adding more reactor types, such as the mixed flow reactor; and adding sizing for the components, as a first step to incorporate TEA models. This open-source tool can help the research community in advancing this promising technology for various applications through a collaborative effort.

Data availability statement

The datasets presented in this study can be found in online repositories. The names of the repository/repositories and accession number(s) can be found in the article/Supplementary Material.

Author contributions

AL: Conceptualization, Data curation, Formal Analysis, Investigation, Methodology, Project administration, Validation, Visualization, Writing – original draft, Writing – review and editing. JM: Investigation, Methodology, Validation, Writing – original draft, Writing – review and editing.

Funding

The author(s) declare that financial support was received for the research and/or publication of this article. This work was authored by the National Renewable Energy Laboratory for the U.S. Department of Energy (DOE) under Contract No. DE-AC36-08GO28308. The authors gratefully acknowledge research

References

Abanades, S., and Flamant, G. (2006). Thermochemical hydrogen production from a two-step solar-driven water-splitting cycle based on cerium oxides. *Sol. Energy* 80, 1611–1623. doi:10.1016/j.solener.2005.12.005

support from the HydroGEN Advanced Water Splitting Materials Consortium, established as part of the Energy Materials Network under the U.S. Department of Energy, Office of Energy Efficiency and Renewable Energy, Fuel Cell Technologies Office, under Contract Numbers DE-EE0010732 and DE-EE0010729.

Acknowledgments

The authors would like to acknowledge the helpful comments and feedback on the model offered by Zahra Hosseinzadeh-Nik. AL would also like to thank Brendan Bulfin for the fruitful discussions on performance indicators and their relations to material properties.

Conflict of interest

The authors declare that the research was conducted in the absence of any commercial or financial relationships that could be construed as a potential conflict of interest.

Generative AI statement

The author(s) declare that no Generative AI was used in the creation of this manuscript.

Any alternative text (alt text) provided alongside figures in this article has been generated by Frontiers with the support of artificial intelligence and reasonable efforts have been made to ensure accuracy, including review by the authors wherever possible. If you identify any issues, please contact us.

Publisher's note

All claims expressed in this article are solely those of the authors and do not necessarily represent those of their affiliated organizations, or those of the publisher, the editors and the reviewers. Any product that may be evaluated in this article, or claim that may be made by its manufacturer, is not guaranteed or endorsed by the publisher.

Supplementary material

The Supplementary Material for this article can be found online at: https://www.frontiersin.org/articles/10.3389/fenrg.2025.1665986/full#supplementary-material

Abanades, S., Legal, A., Cordier, A., Peraudeau, G., Flamant, G., and Julbe, A. (2010). Investigation of reactive cerium-based oxides for H2 production by thermochemical two-step water-splitting. *J. Mater. Sci.* 45, 4163–4173. doi:10.1007/s10853-010-4506-4

- Ackermann, S., Takacs, M., Scheffe, J., and Steinfeld, A. (2017). Reticulated porous ceria undergoing thermochemical reduction with high-flux irradiation. Int. J. Heat Mass Transf. 107, 439–449. doi:10.1016/j.ijheatmasstransfer.2016. 11.032
- Adanez, J., Abad, A., Garcia-Labiano, F., Gayan, P., and De Diego, L. F. (2012). Progress in chemical-looping combustion and reforming technologies. *Prog. energy Combust. Sci.* 38, 215–282. doi:10.1016/j.pecs.2011.09.001
- Bayon, A., de la Calle, A., Stechel, E. B., and Muhich, C. (2022). Operational limits of redox metal oxides performing thermochemical water splitting. *Energy Technol.* 10, 2100222–11. doi:10.1002/ente.202100222
- Bell, I. H., Wronski, J., Quoilin, S., and Lemort, V. (2014). Pure and pseudo-pure fluid thermophysical property evaluation and the open-source thermophysical property library CoolProp. *Industrial and Eng. Chem. Res.* 53, 2498–2508. doi:10.1021/ie40
- Budama, V. K., Brendelberger, S., Roeb, M., and Sattler, C. (2022). Performance analysis and optimization of solar thermochemical water-splitting cycle with single and multiple receivers. *Energy Technol.* 10, 2100220. doi:10.1002/ente.2021 00220
- Bulfin, B. (2019). Thermodynamic limits of countercurrent reactor systems, with examples in membrane reactors and the ceria redox cycle. *Phys. Chem. Chem. Phys.* 21, 2186–2195. doi:10.1039/C8CP07077F
- Bulfin, B., Call, F., Lange, M., Lübben, O., Sattler, C., Pitz-Paal, R., et al. (2015). Thermodynamics of CeO_2 thermochemical fuel production. *Energy and Fuels* 29, 1001-1009. doi:10.1021/ef5019912
- Bulfin, B., Hoffmann, L., de Oliveira, L., Knoblauch, N., Call, F., Roeb, M., et al. (2016). Statistical thermodynamics of non-stoichiometric ceria and ceria zirconia solid solutions. *Phys. Chem. Chem. Phys.* 18, 23147–23154. doi:10.1039/C6CP0 3158G
- Bulfin, B., Miranda, M., and Steinfeld, A. (2021). Performance indicators for benchmarking solar thermochemical fuel processes and reactors. *Front. Energy Res.* 9, 677980–12. doi:10.3389/fenrg.2021.677980
- Carrillo, R. J., and Scheffe, J. R. (2019). Beyond ceria: theoretical investigation of isothermal and near-isothermal redox cycling of perovskites for solar thermochemical fuel production. *Energy and Fuels* 33, 12871–12884. doi:10.1021/acs.energyfuels.9b02714
- Chueh, W. C., Falter, C., Abbott, M., Scipio, D., Furler, P., Haile, S. M., et al. (2010). High-flux solar-driven thermochemical dissociation of CO_2 and H_2O using ceria redox reactions. *Science* 330, 1797–1801. doi:10.1126/science.1197834
- de la Calle, A., Ermanoski, I., and Stechel, E. B. (2022). Towards chemical equilibrium in thermochemical water splitting. part 1: thermal reduction. *Int. J. Hydrogen Energy* 47, 10474–10482. doi:10.1016/j.ijhydene.2021.07.167
- de la Calle, A., Ermanoski, I., Miller, J. E., and Stechel, E. B. (2024). Towards chemical equilibrium in thermochemical water splitting. Part 2: Re-oxidation. *Int. J. Hydrogen Energy* 72, 1159–1168. doi:10.1016/j.ijhydene.2024.05.298
- Ehrhart, B. D., Muhich, C. L., Al-Shankiti, I., and Weimer, A. W. (2016). System efficiency for two-step metal oxide solar thermochemical hydrogen production Part 2: impact of gas heat recuperation and separation temperatures. *Int. J. Hydrogen Energy* 41, 19894–19903. doi:10.1016/j.ijhydene.2016.07.110
- Fan, L.-S. (2011). Chemical looping systems for fossil energy conversions. John Wiley and Sons.
- Gokon, N., Mataga, T., Kondo, N., and Kodama, T. (2011). Thermochemical two-step water splitting by internally circulating fluidized bed of NiFe2O4 particles: successive reaction of thermal-reduction and water-decomposition steps. *Int. J. Hydrogen Energy* 36, 4757–4767. doi:10.1016/j.ijhydene.2011.01.076
- Goodwin, D. G., Moffat, H. K., Schoegl, I., Speth, R. L., and Weber, B. W. (2023). Cantera: an object-oriented software toolkit for chemical kinetics, thermodynamics, and transport processes. doi:10.5281/zenodo.8137090
- Hao, Y., Yang, C.-K., and Haile, S. M. (2014). Ceria–zirconia solid solutions ($Ce_{1-x}Zr_xO_{2-\delta}$, $x\leq 0.2$) for solar thermochemical water splitting: a thermodynamic study. *Chem. Mater.* 26, 6073–6082. doi:10.1021/cm503131p
- Hathaway, B. J., Bala Chandran, R., Gladen, A. C., Chase, T. R., and Davidson, J. H. (2016). Demonstration of a solar reactor for carbon dioxide splitting via the isothermal ceria redox cycle and practical implications. *Energy and Fuels* 30, 6654–6661. doi:10.1021/acs.energyfuels.6b01265
- Kathe, M., Empfield, A., Sandvik, P., Fryer, C., Zhang, Y., Blair, E., et al. (2017). Utilization of CO₂ as a partial substitute for methane feedstock in chemical looping methane–steam redox processes for syngas production. *Energy and Environ. Sci.* 10, 1345–1349. doi:10.1039/c6ee03701a
- $Kee, J., and Penev, M. M. (2023). \ ProFAST production financial analysis scenario tool SWR-23-88. \ Golden, CO: Tech. \ rep., National Renewable Energy Laboratory.$
- Lany, S. (2024). Chemical potential analysis as an alternative to the van't hoff method: hypothetical limits of solar thermochemical hydrogen. *J. Am. Chem. Soc.* 146, 14114–14127. doi:10.1021/jacs.4c02688
- Li, S., Wheeler, V. M., Kreider, P. B., Bader, R., and Lipiński, W. (2018a). Thermodynamic analyses of fuel production via solar-driven non-stoichiometric metal

- oxide redox cycling. Part 2. Impact of solid–gas flow configurations and active material composition on system-level efficiency. *Energy and Fuels* 32, 10848–10863. doi:10.1021/acs.energyfuels.8b02082
- Li, S., Wheeler, V. M., Kreider, P. B., and Lipiński, W. (2018b). Thermodynamic analyses of fuel production via solar-driven non-stoichiometric metal oxide redox cycling. Part 1. Revisiting flow and equilibrium assumptions. *Energy and Fuels* 32, 10838–10847. doi:10.1021/acs.energyfuels.8b02081
- Lidor, A. (2024). Hydrogen–steam separation using mechanical vapor recompression cycle. *Int. J. Hydrogen Energy* 94, 664–668. doi:10.1016/j.ijhydene.2024.11.040
- Lidor, A., and Bulfin, B. (2024). A critical perspective and analysis of two-step thermochemical fuel production cycles. *Sol. Compass* 11, 100077. doi:10.1016/j.solcom.2024.100077
- Lidor, A., and Zimmermann, L. (2023). Experimental demonstration of high-temperature heat recovery in a solar reactor. *Sol. Energy* 262, 111915. doi:10.1016/j.solener.2023.111915
- Lidor, A., Fend, T., Roeb, M., and Sattler, C. (2021). High performance solar receiver-reactor for hydrogen generation. *Renew. Energy* 179, 1217–1232. doi:10.1016/j.renene.2021.07.089
- Lidor, A., Aschwanden, Y., Häseli, J., Reckinger, P., Haueter, P., and Steinfeld, A. (2023). High-temperature heat recovery from a solar reactor for the thermochemical redox splitting of $\rm H_2O$ and $\rm CO_2$. Appl. Energy 329, 120211. doi:10.1016/j.apenergy.2022.120211
- Ma, Z., Gifford, J., Wang, X., and Martinek, J. (2023). Electric-thermal energy storage using solid particles as storage media. *Joule* 7, 843–848. doi:10.1016/j.joule.2023.03.016
- Mao, Y., Gao, Y., Dong, W., Wu, H., Song, Z., Zhao, X., et al. (2020). Hydrogen production via a two-step water splitting thermochemical cycle based on metal oxide–a review. *Appl. energy* 267, 114860. doi:10.1016/j.apenergy.2020.114860
- McCord, D. C., Gager, E. J., Wang, X., Johnson, T. L., Beachy, J. S., King, K. A., et al. (2024). Solar thermochemical redox cycling using ga- and al-doped lsm perovskites for renewable hydrogen production. *J. Phys. Chem. C* 128, 15796–15806. doi:10.1021/acs.jpcc.4c02797
- McDaniel, A. H., Miller, E. C., Arifin, D., Ambrosini, A., Coker, E. N., O'Hayre, R., et al. (2013). Sr- and Mn-doped LaAlO3- δ for solar thermochemical H 2 and CO production. *Energy Environ. Sci.* 6, 2424–2428. doi:10.1039/c3ee 41372a
- Nakamura, T. (1977). Hydrogen production from water utilizing solar heat at high temperatures. Sol. Energy 19, 467–475. doi:10.1016/0038-092X(77)90102-5
- Panlener, R. J., Blumenthal, R. N., and Garnier, J. E. (1975). A thermodynamic study of nonstoichiometric cerium dioxide. *J. Phys. Chem. Solids* 36, 1213–1222. doi:10.1016/0022-3697(75)90192-4
- Patankar, A. S., Wu, X.-Y., Choi, W., Tuller, H. L., and Ghoniem, A. F. (2022). A reactor train system for efficient solar thermochemical fuel production. *J. Sol. Energy Eng.* 144, 061014–12. doi:10.1115/1.4055298
- Romero, M., and Steinfeld, A. (2012). Concentrating solar thermal power and thermochemical fuels. *Energy Environ. Sci.* 5, 9234–9245. doi:10.1039/c2ee 21275g
- Scheffe, J. R., and Steinfeld, A. (2014). Oxygen exchange materials for solar thermochemical splitting of $\rm H_2O$ and $\rm CO_2$: a review. *Mater. Today* 17, 341–348. doi:10.1016/j.mattod.2014.04.025
- Siegel, N. P., Miller, J. E., Ermanoski, I., Diver, R. B., and Stechel, E. B. (2013). Factors affecting the efficiency of solar driven metal oxide thermochemical cycles. *Industrial and Eng. Chem. Res.* 52, 3276–3286. doi:10.1021/ie400193q
- Steinfeld, A. (2005). Solar thermochemical production of hydrogen a review. Sol. Energy 78, 603–615. doi:10.1016/j.solener.2003.12.012
- Thanda, V., Fend, T., Laaber, D., Lidor, A., von Storch, H., Säck, J., et al. (2022). Experimental investigation of the applicability of a 250 kW ceria receiver/reactor for solar thermochemical hydrogen generation. *Renew. Energy* 198, 389–398. doi:10.1016/j.renene.2022.08.010
- The MathWorks Inc. (2023). MATLAB version: 23.2.0.2428915 (R2023b) Update 4.
- Tran, J. T., Warren, K. J., Mejic, D., Anderson, R. L., Jones, L., Hauschulz, D. S., et al. (2023). Pressure-enhanced performance of metal oxides for thermochemical water and carbon dioxide splitting. *Joule* 7, 1759–1768. doi:10.1016/j.joule.2023.07.016
- Vieten, J., Bulfin, B., Huck, P., Horton, M., Guban, D., Zhu, L., et al. (2019). Materials design of perovskite solid solutions for thermochemical applications. *Energy and Environ. Sci.* 12, 1369–1384. doi:10.1039/c9ee00085b
- Warren, K. J., and Weimer, A. W. (2022). Solar thermochemical fuels: present status and future prospects. *Sol. Compass* 1, 100010. doi:10.1016/j.solcom.2022. 100010
- Warren, K. J., Tran, J. T., and Weimer, A. W. (2022). A thermochemical study of iron aluminate-based materials: a preferred class for isothermal water splitting. *Energy Environ. Sci.* 15, 806–821. doi:10.1039/d1ee02679h
- Wexler, R. B., Gautam, G. S., Bell, R. T., Shulda, S., Strange, N. A., Trindell, J. A., et al. (2023). Multiple and nonlocal cation redox in ca-ce-ti-mn oxide perovskites

for solar thermochemical applications. $Energy\ and\ Environ.\ Sci.\ 16,\ 2550-2560.$ doi:10.1039/d3ee00234a

Wilson, S. A., Sarsam, P. W., Stechel, E. B., and Muhich, C. L. (2024). Extracting metal oxide redox thermodynamics from tga measurements requires moving beyond the linearized van 't hoff approach. *Front. Energy Res.* 12, 1470010–1472024. doi:10.3389/fenrg.2024.1470010

Yang, C.-K., Yamazaki, Y., Aydin, A., and Haile, S. M. (2014). Thermodynamic and kinetic assessments of strontium-doped lanthanum manganite perovskites for two-step thermochemical water splitting. *J. Mater. Chem. A* 2, 13612–13623. doi:10.1039/C4TA02694B

Zang, G., Sun, P., Elgowainy, A. A., Bafana, A., and Wang, M. (2021). Performance and cost analysis of liquid fuel production from h2 and co2 based on the fischer-tropsch process. *J. CO2 Util.* 46, 101459. doi:10.1016/j.jcou.2021.101459

Zhao, X., Zhou, H., Sikarwar, V. S., Zhao, M., Park, A.-H. A., Fennell, P. S., et al. (2017). Biomass-based chemical looping technologies: the good, the bad and the future. *Energy and Environ. Sci.* 10, 1885–1910. doi:10.1039/c6ee03718f

Zinkevich, M., Djurovic, D., and Aldinger, F. (2006). Thermodynamic modelling of the cerium-oxygen system. *Solid State Ionics* 177, 989–1001. doi:10.1016/j.ssi.2006.02.044

Nomenclature

Roman symbols

 $\mathbf{HHV} \qquad \qquad \text{Higher heating value, J mol}^{-1}$

 $j_{\rm A}$ Molar flux of species A from flow 1 to flow 2, mol m $^{-1}$ s $^{-1}$

 K Equilibrium constant

 \dot{n} Molar flow rate, mol s⁻¹

 p Reactor pressure, Pa

 p° Reference pressure, Pa

 p_{O_2} Oxygen partial pressure, Pa

 $oldsymbol{q}$ Specific heat, J mol $^{-1}$ $\dot{oldsymbol{Q}}$ Heat transfer rate, W

R Universal gas constant, kJ mol⁻¹ K⁻¹

T Temperature, K w Specific work, J mol⁻¹

 \dot{W} Power, W

X Conversion extentx Mole fraction

Greek symbols

 δ Deviation from non-stoichiometry

 $\Delta \delta$ Extent of reduction

 $\Delta\phi$ Change in oxygen content in the redox-active material

 ΔG Gibbs free energy of reaction, kJ mol⁻¹

ε Heat recovery effectiveness

η System efficiency

 κ Species exchange coordinate μ Chemical potential, kJ mol⁻¹

 ω Ratio between gas and solid molar flow rates

 ϕ Oxygen content in the redox-active material

Subscripts

f final state fuel Fuel

g gas phasein Inlet

MO Metal oxide
out Outlet
ox Oxidation
prod Product
reac Reactant
red Reduction

eq Required for the entire process

sg Sweep gass solid phase

Superscripts

ox Oxidation
red Reduction